SENSORS

A highly sensitive, self-powered triboelectric auditory sensor for social robotics and hearing aids

Hengyu Guo[1,2,3]*, Xianjie Pu[1]*, Jie Chen[1]*, Yan Meng[1], Min-Hsin Yeh[4], Guanlin Liu[1,2], Qian Tang[1], Baodong Chen[2], Di Liu[2], Song Qi[1], Changsheng Wu[3], Chenguo Hu[1†], Jie Wang[2†], Zhong Lin Wang[2,3†]

The auditory system is the most efficient and straightforward communication strategy for connecting human beings and robots. Here, we designed a self-powered triboelectric auditory sensor (TAS) for constructing an electronic auditory system and an architecture for an external hearing aid in intelligent robotic applications. Based on newly developed triboelectric nanogenerator (TENG) technology, the TAS showed ultrahigh sensitivity (110 millivolts/decibel). A TAS with the broadband response from 100 to 5000 hertz was achieved by designing the annular or sectorial inner boundary architecture with systematic optimization. When incorporated with intelligent robotic devices, TAS demon-strated high-quality music recording and accurate voice recognition for realizing intelligent human-robot interaction. Furthermore, the tunable resonant frequency of TAS was achieved by adjusting the geometric design of inner bound-ary architecture, which could be used to amplify a specific sound wave naturally. On the basis of this unique property, we propose a hearing aid with the TENG technique, which can simplify the signal processing circuit and reduce the power consuming. This work expresses notable advantages of using TENG technology to build a new generation of auditory systems for meeting the challenges in social robotics.

INTRODUCTION

With the fast development of robotics, several grand challenges will be considered by the robotics industry in the next generation (*1*). As the most efficient and straightforward communication channel, one criterion for robotic auditory systems requires the robot not only to listen to our instructions but also to perceive our vocal intonations, which means an intelligent mobile robot truly integrated with our social life, showing empathy and natural social behaviors (*1*–*3*). To facilitate social interaction with robotics, the auditory sensor in a robotic system should mimic human senses by being more sensitive, including a broader frequency response. In addition, more than 10% of the global population suffers from hearing impairments (*4*, *5*), and those people are potential beneficiaries of service robotics. Commonly, people with impaired hearing are unable to hear one or several specific frequency regions (*6*, *7*). The purpose of an external hearing aid is to amplify the specific impaired sound regions to audible levels (*8*–*10*). Therefore, auditory sensors with frequency selectivity as hearing aid devices for the hearing-impaired could supplement human-robot social interactions. However, deep social interaction between robots and humans would bring about power/energy challenges because of abundant powerful sensors (*1*). A traditional auditory sensor often uses a microphone that combines precise signals with a processing circuit, thus increasing the power consumption and shortening the operation period (*7*). Besides developing new energy-storing technology, developments in self-powered auditory sensors with high sensitivity, broader frequency response, and frequency selectivity could play a key role in addressing the social interaction and power/energy challenges of robotics (*1*, *11*, *12*).

To address these issues, several research groups have developed a kind of self-powered auditory platform based on the piezoelectric effect (*13*–*16*). Different from traditional microphone technologies (*17*–*19*), these trapezoid-structured sensors (*13*–*16*) have several advantages, such as self-powering (integrated sensing and signal conversion), broader frequency response, and frequency selectivity. However, the piezoelectric sensors have a low output signal and a relatively high frequency response region in comparison with the frequency range of human voices. In addition, the multiple signal channels, complicated fabrication process, and piezoelectric materials make them costly (*14*). These deficiencies limit the application of piezoelectric auditory sensors to social interaction between humans and robots.

Recently, a triboelectric nanogenerator (TENG), based on the coupling of triboelectrification and electrostatic induction, has been developed as a new electromechanical conversion technology (*20*–*25*), which exhibits wide applications in both energy harvesting (*26*–*31*) and self-powered mechanical sensing (*32*–*36*). Based on its unique working mechanism, triboelectric active sensors have shown ultrahigh sensitivity to mechanical stimulus, detecting motion on the scale of hundreds of nanometers (*37*) and monitoring extremely weak arterial pulses from the human body (*32*, *33*). In addition, by taking advantage of various materials and simple structures, Fan *et al.* (*38*) demonstrated a triboelectric acoustic energy-harvesting device. Furthermore, a triboelectric multichannel trapezoid beam–structured artificial membrane has been developed to mimic cochlear tonotopy and showed a high response to the lower frequency range of the human voice (*39*). With these capabilities, a triboelectric auditory sensor (TAS) may provide a simple solution to the social interaction and power/energy challenges of robotics.

Here, we report a circular-type, easy-fabrication, single-channel, and self-powered TAS for building an electronic hearing system for both robotics and human beings. The performance of TAS was systematically studied both theoretically and experimentally. TAS showed ultrahigh sensitivity (to 110 mV/dB) and a broad frequency response from 100 to 5000 Hz, almost covering the frequency range of the human voice. It is demonstrated to be a low-cost, energy-efficient, and

[1]Department of Applied Physics, State Key Laboratory of Power Transmission Equipment and System Security and New Technology, Chongqing University, Chongqing 400044, P. R. China. [2]Beijing Institute of Nanoenergy and Nanosystems, Chinese Academy of Sciences, Beijing 100083, P. R. China. [3]School of Materials Science and Engineering, Georgia Institute of Technology, Atlanta, GA 30332, USA. [4]Department of Chemical Engineering, National Taiwan University of Science and Technology, Taipei 10607, Taiwan.
*These authors contributed equally to this work.
†Corresponding author. Email: hucg@cqu.edu.cn (C.H.); wangjie@binn.cas.cn (J.W.); zhong.wang@mse.gatech.edu (Z.L.W.)

high-fidelity auditory platform for social robotics interaction. By adjusting the annular/sectorial inner boundary architecture, we achieved a tailored frequency response from the sensor itself and demonstrated the application as a hearing aid device for recovering hearing-impaired people, thus supplementing human-robot interaction from the auditory sense. This work exhibits a prospective application of the TENG-based sensor for meeting the future challenges of robotics.

RESULTS

Basic structure and working mechanism of TAS

TENG is the technology for constructing the electronic hearing system. Figure 1A proposes the triboelectric cochlea (TEC) device for an intelligent auditory system. The TEC device is integrated inside the artificial ear. The detailed layer-by-layer structural scheme of the basic TAS is shown in Fig. 1B. The circular-type device mainly consists of a fluorinated ethylene propylene (FEP)–covered upper electrode (with several hole channels), a certain gap-created spacer (thickness of ~100 μm), and a Kapton (DuPont) membrane connected with the bottom electrode. The outer edge of the Kapton membrane is fixed by annular acrylic sheet, and the inner film is free for vibration. Further structure design can be applied to the inner film for frequency response modulation. To enhance the surface charge density for higher sensitivity, we created nanostructure on the FEP surface as shown in Fig. 1C. Because of the simple structure and the properties of selected materials in TENG technology, the device can be tiny, thin in size, and even transparent in appearance for wide applications (see photograph of the basic device in Fig. 1D). The detailed device fabrication process is described in Materials and Methods.

The working principle of the TAS for acoustic wave sensing can be elucidated from two aspects: Namely, acoustic wave induces membrane deformation, and membrane vibration causes electric signal output. Figure 1E illustrates the cross section of TAS components. When there exists an acoustic source, the generated air pressure difference drives the Kapton membrane to vibrate. As a thin circular membrane with fixed edge, the steady-state vibration mode should satisfy the following Helmholtz equation (*40*) and boundary condition (in the polar coordinates)

$$\nabla^2 U + k^2 U = \frac{1}{\rho}\frac{\partial}{\partial \rho}\left(\rho \frac{\partial U}{\partial \rho}\right) + \frac{1}{\rho^2}\frac{\partial^2 U}{\partial \theta^2} + \frac{\omega^2}{c^2}U = 0 \quad \rho < D/2 \qquad (1)$$

$$U = 0 \quad \rho = D/2 \qquad (2)$$

where U is the envelope of the membrane, ρ is the polar radius, k represents the wave number (equal to $\frac{\omega}{c}$), ω is the angular frequency, D is the diameter of the membrane, $c = \sqrt{\frac{T}{\sigma}}$ is the wave velocity, and T and σ represent the stretching force and the surface mass density, respectively, of the membrane. The solution of Eq. 1 can be expressed as

$$U = \left[A_1 J_m\left(\frac{\omega\rho}{c}\right) + A_2 Y_m\left(\frac{\omega\rho}{c}\right)\right]\sin(n\theta + \varphi) \qquad (3)$$

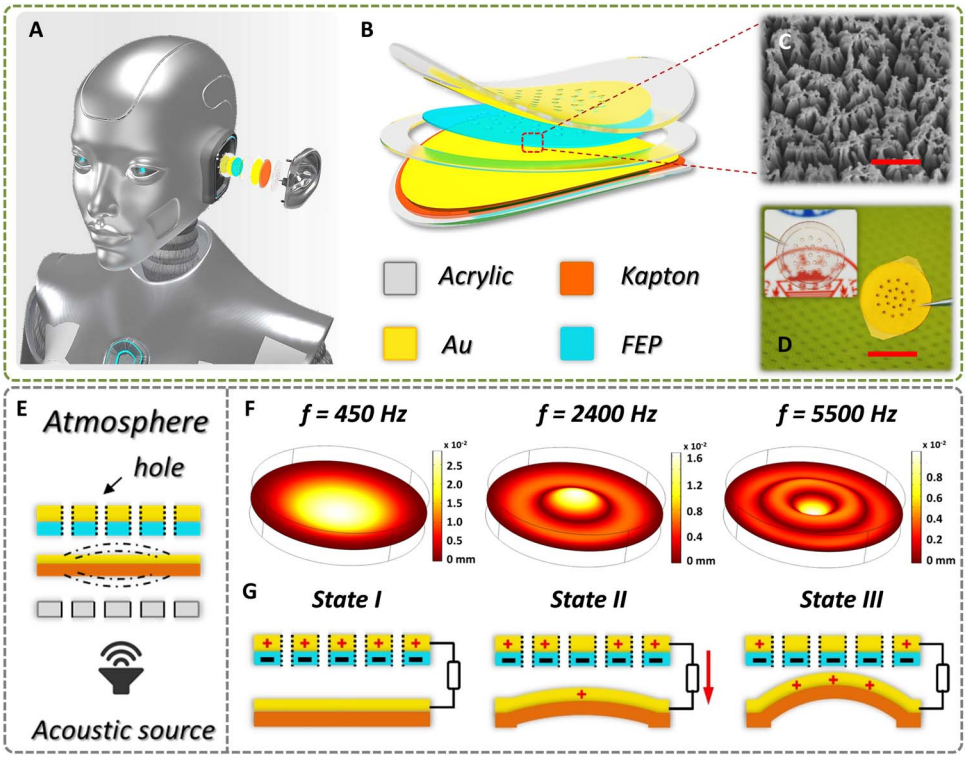

Fig. 1. Structure and mechanism of the TAS. (**A**) Proposed image of triboelectric auditory system for a robot. (**B**) Basic structure scheme of the TAS. (**C**) Scanning electron microscopy image of the FEP surface. Scale bar, 1 μm. (**D**) Digital photograph of the acrylic-based device and the transparent device. Scale bar, 1 cm. (**E**) Cross-sectional scheme of the working components. (**F**) Vibration patterns of Kapton film under different frequencies (simulated using COMSOL under sound pressure of 5 Pa). (**G**) Schematic charge distribution during the film vibration.

where A_1 and A_2 are two undetermined coefficients and $J_m(x)$ and $Y_m(x)$ are the m-step first-type and second-type Bessel functions (*40*), respectively, and n is an integer. From Eq. 3, various vibration modes are formed under a certain acoustic frequency. Using the finite element analysis method (COMSOL Multiphysics), we simulated deforming displacements of a circular membrane under three certain acoustic frequencies (Fig. 1F). Figure S1 presents various vibration patterns. Usually, the first-order vibration mode provides the largest mechanical deformation; therefore, we mainly focused on modulating this mode for broadening response frequency band. The deformation of the Kapton membrane brings about the contact triboelectrification between FEP and bottom electrode under a certain sound frequency, pressure level, and gap distance; thus, negatively bonded charges can be formed on FEP surface because of differences in electron affinity (*41*). When the air pressure changes, the mechanical motion–induced separation between the charged FEP and the bottom electrode results in a flow of electrons from upper electrode to bottom electrode driven by electrostatic induction. The return contact between FEP and bottom electrode generates backflow electric signal

output. Figure 1G illustrates three states of the schematic charge distribution under the short-circuit condition. The potential distribution under the open-circuit condition is simulated as depicted in fig. S2. This electric output mechanism results from the coupling of triboelectrification and electrostatic induction.

Fundamental characteristics of TAS

We systematically investigated the sensing performance and the characteristics of basic TAS with different geometric parameters. Because of its suitable mechanical properties, Kapton film was chosen as the membrane material for fabricating the device. For a circular membrane, the diameter and the thickness are two key parameters affecting the frequency response (Fig. 2A). A typical voltage signal of the TAS (diameter, 15 mm; thickness, 75 μm; gap, 0.2 mm) under the acoustic frequency range from 100 to 5000 Hz is presented in Fig. 2B. Because 100 to 5000 Hz is the basic frequency range of communication for human beings (table S1 shows the sound and corresponding frequency range), we based the measurement and modulation mainly on this frequency range. From the typical electric signal, TAS is self-powered with about 1.2-V high electric output (100-dB sound pressure level) and shows a resonant feature. The high output over the baseline ensured the high sensitivity of the device, but the resonant property led to a narrow frequency band, which needed to be broadened. Deriving from Fourier transform, the frequency spectra of TAS with different membrane diameters and thicknesses are depicted in Fig. 2 (C and D). The experimental results indicate that (i) TAS with a larger membrane

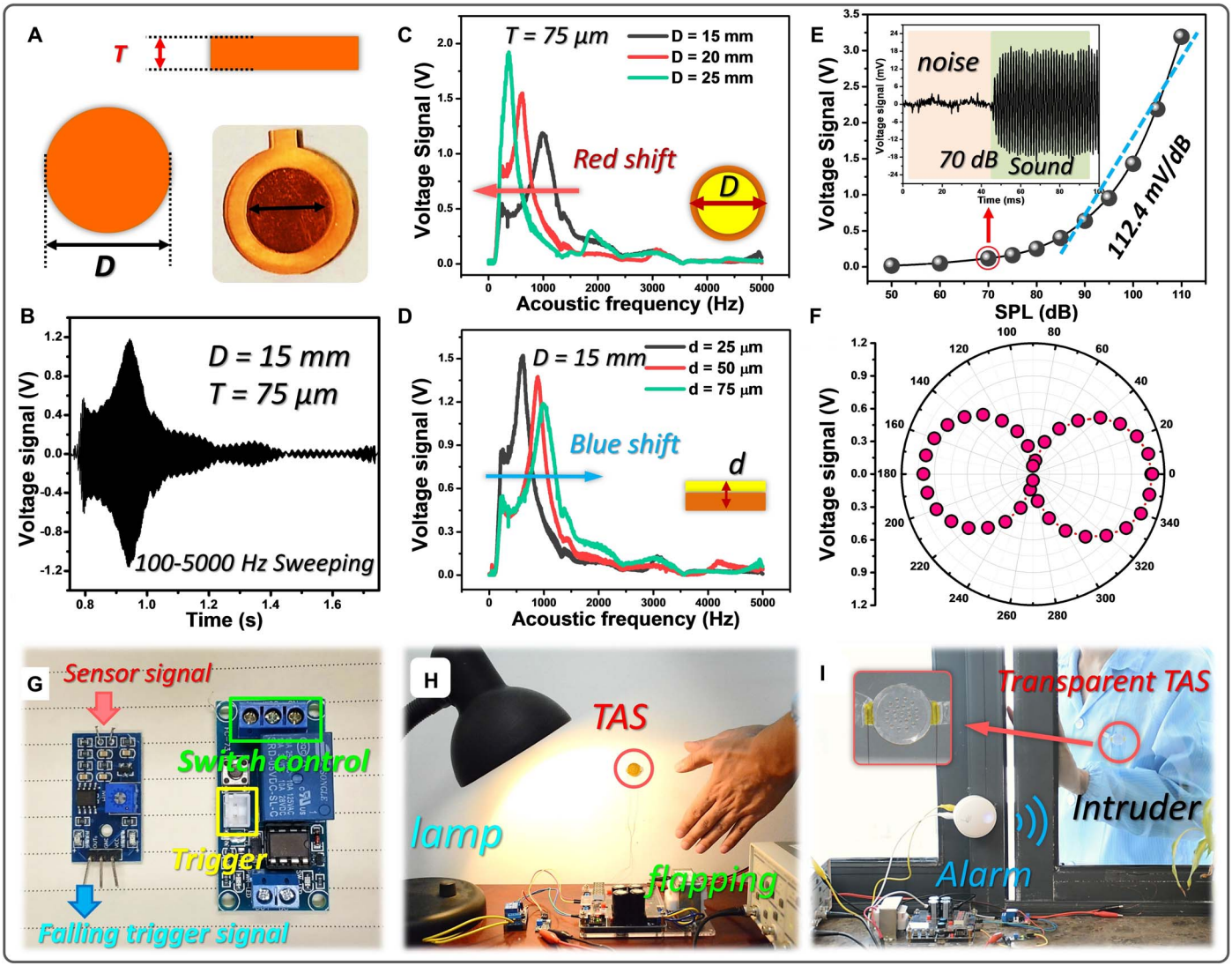

Fig. 2. Characterization of acoustic response performance of the TAS with different geometric designs and their practical applications. (**A**) Schematic illustration of TAS with various geometric designs. (**B**) Voltage signal measured from a TAS (gap distance, 0.2 mm; sweeping frequency range, 100 to 5000 Hz; sound intensity, 100 dB_{SPL}). The frequency spectrum of TAS derived through Fourier transform (device gap distance, 0.2 mm) when varying (**C**) diameter and (**D**) thickness of the Kapton membrane. (**E**) The acoustic response of a TAS (D = 15 mm, d = 75 μm) under various sound intensities. Inset: Acoustic response difference between the noise and specific sound signal (around 60 dB). (**F**) Shape-dependent directional patterns of the TAS (D = 15 mm, d = 75 μm). (**G**) Electronic module used for potential application demonstration. (**H**) Demonstration of TAS as a sensitive sound switch control. (**I**) Demonstration of a transparent TAS for an antitheft system.

diameter held a lower resonant frequency and higher electric output, and (ii) a thicker membrane resulted in a higher resonant frequency and lower electric output. According to Eq. 3 and the boundary condition, the resonant frequency and the corresponding vibration mode of the fixed circular membrane can be expressed as

$$\omega^{(m,n)} = \frac{2c\mu_{m,n}}{D} \quad (4)$$

$$U = J_m\left(\mu_{m,n}\frac{\rho}{D}\right)\sin(n\theta + \varphi) \quad (5)$$

where m and n represent various vibration modes and $\mu_{m,n}$ represents the zero point of Bessel function J_m, which means that $J_m(\mu_{m,n}) = 0$. When $m = 1$ and $n = 0$, J_m represents the first-order centrosymmetric vibration mode on which we are focused. The detailed discussion is shown in note S1. Equation 5 presents a qualitative relation among resonant frequency, membrane diameter, and membrane thickness (affects the stretching force), which are consistent with the experimental results. Moreover, finite element analysis was also carried out for simulating average z-displacement of the membrane; the quantitative results exhibit the same frequency response trend, and the higher electric output is owing to the larger deformation (figs. S3 and S4). These theoretical analyses provide fundamental guidance for modulating the frequency response of TAS.

As a high electric output acoustic sensor, the sensitivity and directional response should be studied. Figure 2E plots the output amplitudes of a TAS device (diameter, 15 mm; thickness, 50 μm) under its resonance frequency, whereas the sound pressure level (SPL) varied from 50 to 110 dB. The output shows an exponential growth with the sound intensity. In the frequency region of 85 to 110 dB, a high average sensitivity of 112.4 mV/dB was achieved. Even in a weak voice, the electric signal output was still distinguished from the noise (as shown in the inset). The directional sound response property is depicted in Fig. 2F, where a butterfly-shaped directional pattern with mirror symmetry can be observed, which provides a wide-angle range for acoustic sensing. We note that the gap distance between the membrane and upper electrode plays a key role in both miniaturization and stability of the device. Figure S5 presents the long-term stability test of TAS (membrane diameter, 20 mm; membrane thickness, 50 μm) under two different gap distances, and fig. S6 shows the measured membrane displacement under controlled sound stimulus. These results indicate that a suitable gap distance would ensure the contact between the membrane and FEP under a certain sound frequency and pressure level, which introduces charge replenishment during working, thus making the device stable. We also carried out the miniaturization of the sensor down to 5 mm in diameter (fig. S7). By combining the results in Fig. 2D, we found that the output could be kept at a relatively high level when miniaturizing the device by adjusting the gap distance and membrane thickness. With the above features, a highly sensitive and unique sound control system can be set up by the basic TAS. Photographs (Fig. 2G) of the electronic module show a trigger signal transform module and a latching relay. The signal process of the sound control system and electric circuit is measured stepwise and depicted in fig. S8. Figure 2H demonstrates the use of TAS for effectively controlling the on/off state of a desk lamp (movie S1). In addition, using the transparent TAS, we developed a sound-triggered antitheft system (Fig. 2I). When an intruder unlocked the window, a tiny voice triggered the alarm by the device stuck on the glass (movie S2).

Structure design for achieving a frequency response–tunable TAS

In an auditory system for human-robot interaction, broadband frequency response is a substantial feature for TAS. For traditional artificial cochlea, researchers commonly use piezoelectric materials with a trapezoid membrane to achieve the broadband response or frequency selectivity (*13*–*15*). However, the fabrication process is complicated with multiple channels, the sensitivity is relatively low (only microvolts level), and the response frequency region is relatively high—beyond basic human communication. Benefiting from TENG technology, we developed a circular-type, single-channel, low/medium frequency region response–tunable TAS with easy fabrication and high sensitivity. From the Helmholtz equation, if we introduce an inner boundary condition to the membrane, there will be more than one vibration mode at a certain frequency. That is, a multiresonant frequency band can be achieved, which leads to the broadband frequency response of the device. Owing to the simple device structure based on TENG technology, we proposed an annular inner boundary architecture (D_2, diameter of the inner boundary) (Fig. 3A). With the existence of such an inner boundary, the original circular membrane is divided into an annular one (D_1, outer diameter; D_2, inner diameter) and a smaller circular one (D_2, diameter). To clarify the vibration property of the annular membrane, we give a detailed calculation. For a circumference-fixed annular membrane (Fig. 3A, top), the boundary condition satisfies

$$U(D_1/2, \theta) = 0, U(D_2/2, \theta) = 0, \text{ and } U(\rho, 0) = U(\rho, 2\pi) \quad (6)$$

Deriving from Helmholtz Eq. 1, the resonant frequency and corresponding vibration mode of the annular membrane can be expressed as

$$\omega^{(m,n)} = \lambda_{m,n} \cdot c \quad (7)$$

$$U = \left[J_m(\lambda_{m,n}\rho) - \frac{J_m(\lambda_{m,n}D_2)}{Y_m(\lambda_{m,n}D_2)} \cdot Y_m(\lambda_{m,n}\rho)\right]\sin(n\theta + \varphi) \quad (8)$$

where $\lambda_{m,n}$ is the m-step zero point for Bessel function, which is determined by D_1, D_2, and the vibration mode. The detailed derivation process and various vibration patterns for annular membrane are presented in note S2 and fig. S9, respectively. Through experimental testing (a frequency sweeping from 100 to 5000 Hz), we observed the expected resonant frequency response of the single annular membrane–based TAS (D_1 = 35 mm, D_2 = 17 mm, T = 50 μm) with a signal amplitude of more than ~1 V (Fig. 3B). We also studied the theoretical (fig. S10B) and the experimental (Fig. 3C) frequency spectra with various inner diameters, and the results indicate that a larger inner diameter led to blue shifting of the resonant frequency peak, whereas the corresponding circular membrane showed red shifting behavior (fig. S10C and Fig. 2C). By completing annular and circular part, the entire membrane with annular boundary (Fig. 3A, bottom) demonstrated broadband frequency response and tunable resonant frequency region features. Figure 3D exhibits the electric output signal comparison between a basic TAS (D_1 = 35 mm) and the TAS with annular architecture (D_1 = 35 mm and D_2 = 16 mm). Two resonant frequency regions can be observed, and the frequency band is largely broadened by introducing the inner boundary.

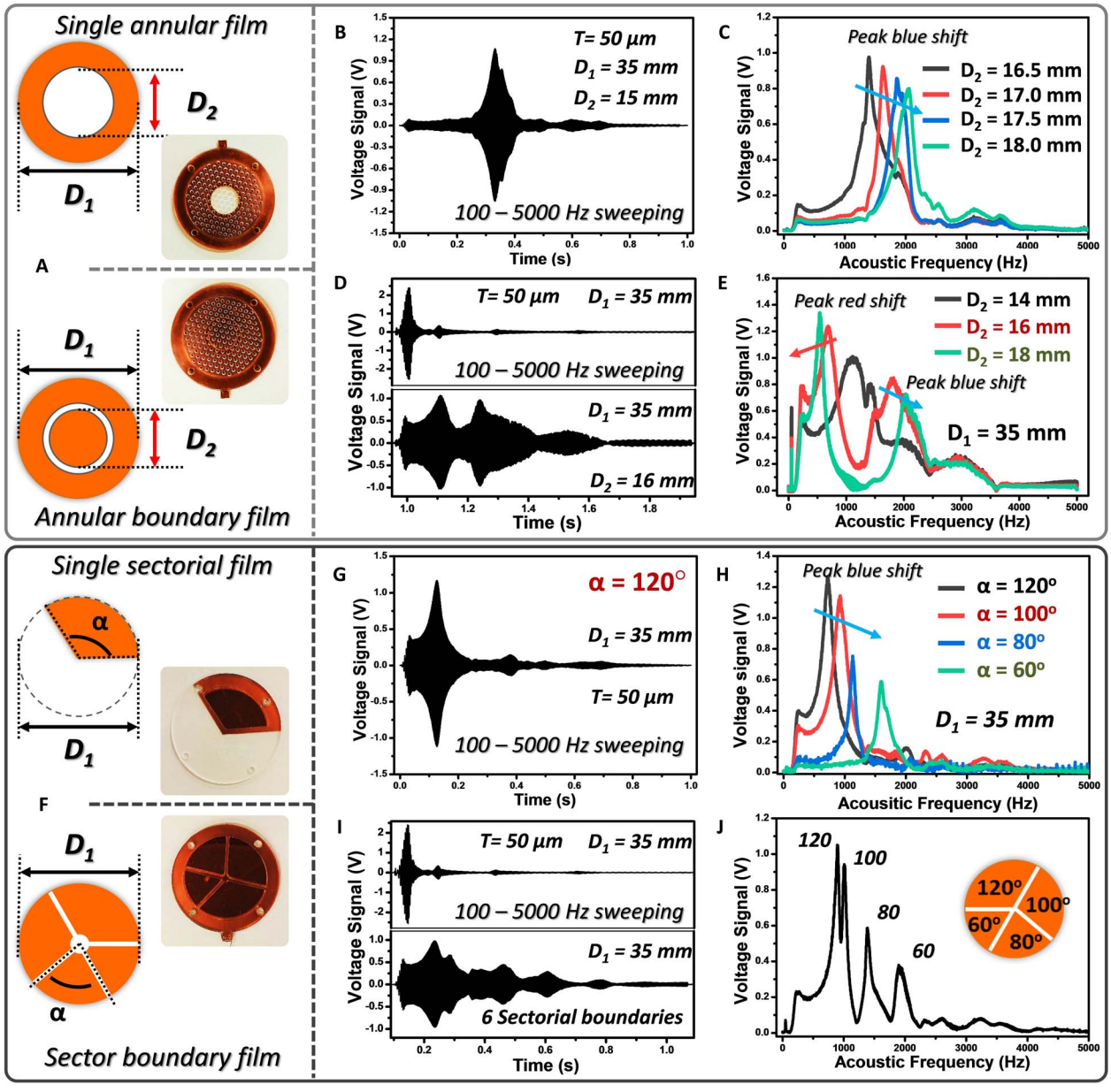

Fig. 3. Inner boundary architecture design for frequency response–tunable TAS. (**A**) Schematic illustrations and photographs of the annular membrane (top) and circular membrane with annular boundary (bottom). (**B**) Voltage signal measured from the annular membrane–based device (D_1 = 35 mm; D_2 = 17.5 mm; sweeping frequency range, 100 to 5000 Hz; sound intensity, 100 dB_{SPL}). (**C**) Frequency spectra of the annular TAS with various inner diameters. (**D**) Comparison of voltage signal output for a circular membrane device with/without annular boundary architecture. (**E**) Frequency spectra of TAS with different annular inner boundary. (**F**) Schematic illustrations and photographs of the sectorial membrane (top) and circular membrane with sectorial boundary (bottom). (**G**) Voltage signal measured from the sectorial membrane–based device (D_1 = 35 mm; α = 120°; sweeping frequency range, 100 to 5000 Hz; sound intensity, 100 dB_{SPL}). (**H**) Frequency spectra of the sectorial TAS with various central angles. (**I**) Comparison of voltage signal output for circular membrane device with/without sectorial boundary architecture. (**J**) Frequency spectrum of the TAS with four sectorial boundaries.

From the frequency spectrum view, two resonant frequency peaks are separated from the spectrum, and one shows red shifting; the other shows blue-shifting behaviors with the increase in inner diameter (Fig. 3E). According to the analysis above, the left-hand side and right-hand side peaks belong to circular membrane and annular membrane, respectively, which match well with the simulated results in fig. S10 (D and E).

Second, we designed a sectorial inner boundary architecture, considering the circular device type. With this boundary condition, the original circular membrane can be divided into several sectorial ones with devisable central angle (α) (Fig. 3D). Similarly, it is necessary to study the vibration features of the sectorial membrane individually (Fig. 3D, top). For this case, the boundary condition of a circumference-fixed sectorial film should be

$$U(D_1/2, \theta) = 0, \;\; U(\rho, 0) = U(\rho, \alpha) = 0 \qquad (9)$$

Deriving from Helmholtz Eq. 1, the resonant frequency and corresponding vibration mode are obtained:

$$\omega^{(m,n)} = \frac{2c\beta_{m,n}}{D_1} \tag{10}$$

$$U = J_m\left(\beta_{m,n}\frac{\rho}{D}\right)\sin\left(\frac{k\pi}{\alpha}\theta + \varphi\right) \tag{11}$$

where $\beta_{m,n}$ is the m-step zero point for Bessel function, which would be determined by α and the vibration mode. The detailed derivation process and the vibration patterns for the sectorial membrane are depicted in note S3 and fig. S11, respectively. The typical electric output signal (Fig. 3G) of a sectorial membrane–based TAS (D_1 = 35 mm, α = 120°, T = 50 μm) also revealed an expected resonant response property. From the view of frequency domain, the resonant frequency region showed blue-shifting behavior as the central angle decreased (Fig. 3H), which is consistent with the simulated results in fig. S12B. Therefore, the TAS with multiple sectorial inner boundaries (Fig. 3F, bottom) exhibited multiple tunable resonant frequency responses with devisable central angles. With a certain device size, we compared electric output signals between a basic TAS (D_1 = 35 mm) and a TAS with six sectorial architectures (α_1 = 100°, α_2 = 80°, α_3 = 60°, α_4 = 50°, α_5 = 40°, and α_6 = 30°) (Fig. 3I), from which multiple resonant frequency bands can be observed, and the frequency band is largely broadened by introducing the inner boundary. For a clear view, the frequency spectrum of the TAS with four sectorial boundaries is also presented (Fig. 3J), from which four resonant peaks can be observed, and each peak can be marked to the corresponding sectorial part according to the simulated result in fig. S12C.

In addition, in the fabrication process, to introduce the inner boundary, a perforated circular acrylic sheet should be used to hold the framework (fig. S13), which creates cavities between the membrane and the perforated sheet. To study the effect of Helmholtz resonance (*42*) on the membrane, we systematically investigated the single-hole and multihole Helmholtz resonator models both experimentally and theoretically (figs. S14 and S15). Generally, a Helmholtz resonator holds the intrinsic frequency, which would narrow the frequency response of the membrane. This narrowing effect is bad for broadening of the frequency band of TAS; however, it is an effective approach to modulating the frequency bandwidth for specific applications. The detailed results and discussion are presented in note S4. Briefly, frequency spectrum of the TAS can be easily modulated by its structure design and optimization, which is useful for applications.

Applications of TAS in electronic auditory systems of intelligent robots

For intelligent robots, the ear is one of the most notable channels for ensuring human-robot interaction. Benefiting from the working mechanism and structure design, our proposed TAS holds ultrasensitivity and broadband (100 to 5000 Hz) response covering the basic range of human communication, which may be ideal as an auditory platform for imitating the hearing system as a sensor. With a thin and simple structure, a circular-type TAS with one signal channel can be easily equipped onto the ear part of a robot (Fig. 4A). To demonstrate its sensitivity and performance, we used the TAS with an annular inner boundary (D_1 = 35 mm, D_2 = 15 mm, T = 50 μm) to listen to a piece of famous Chinese traditional music, "The Butterfly Lovers," from an electromagnetic loudspeaker. The self-generated high output electric signal and one channel allow easy real-time capture and display of the recorded information via a data acquisition device and personal computer (Fig. 4A) without complex signal processing. The time-domain sound wave signal and the spectrograms for the original music and the recorded music are presented in Fig. 4 (B and C, respectively). The recorded music is highly similar to the original one. Movie S3 demonstrates the listening and recording process by the TAS, which shows relatively high quality and fidelity. In addition, voice recognition is important for personal property security.

Next, we demonstrated the use of TAS for realizing an affiliation between a robot and its master. Because of good acoustic recording performance, we recorded detailed sound information while the administrator (Henry) and the guest (Jerry) said "Hello" (Fig. 4D). Deriving from Fourier transform, Fig. 4E depicts the power spectral density estimation (PSDE) and joint time-frequency analysis (JTFA). The generated voltage signal reflects time-domain acoustic information, the PSDE reflects the acoustic frequency information, and

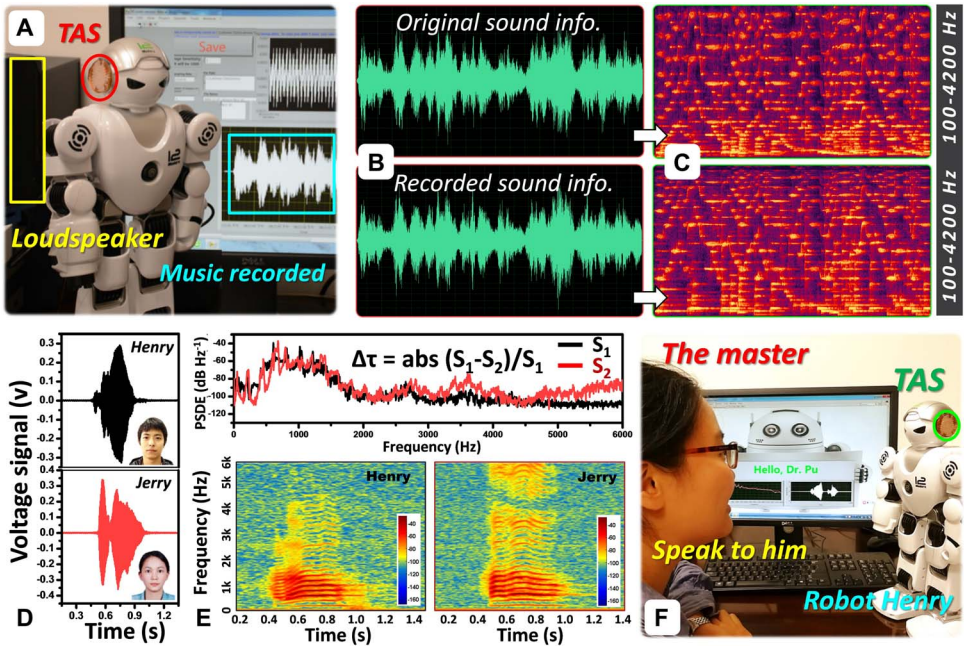

Fig. 4. Application of the TAS for imitating an auditory system. (**A**) Application of TAS for music recording. (**B**) Original music wave and recorded sound wave information. (**C**) Corresponding music and recorded sound spectrograms. (**D**) Voices recorded from two people saying "Hello." (**E**) Power spectral and voice spectrogram of the recorded voices for identification. (**F**) Demonstration of the TAS-based voice recognition system.

the JTFA reflects the joint distribution information of the time domain and the frequency domain. The analysis and comparison between these signals can distinguish the identity of the user. On the basis of the LabVIEW platform, we built a sound recognition system for intelligent robots through comparing the mean deviation $\Delta\tau = \text{abs}\ (S_1 - S_2)/S_1$ between PSDE of the guest (S_2) and preset one (S_1). With the recognition system, the robot only interacted with the administrator (Fig. 4F and movie S4). The demonstration reveals the feasibility of TAS for constructing an electronic auditory system with low-cost and accurate acoustic sensing performance.

Application of TAS in medical hearing aids

Besides the construction of auditory system for robotics, augmenting human hearing using external medical hearing aids also plays a substantial role for supplementing human-robot socialization. To date, roughly 10% of the world population suffers from hearing loss. Hearing loss is typically measured as the shift in auditory threshold parallel to that of a normal ear for detection of a pure tone. In most cases, just one or several specific frequency regions are inaudible for these people. Thus, the intention of hearing aid is to amplify the specific sound signals in such a way that they become audible for hearing-impaired persons (*37*, *39*). Table S2 presents different levels of hearing loss. A traditional hearing aid consists of a microphone-based multichannel sound receiver, a signal-processing circuit, and an in-ear loudspeaker (Fig. 5B). It provides a good solution; however, the stigma of wearing a hearing aid and the expensive cost of the device reduce the number of people who use it. According to the analysis of the TAS spectrum, the resonant feature could enhance the specific frequency region naturally, which may provide an approach for a new type of hearing aid. The single-channel and self-powered features can simplify the signal-processing circuit, thus minimizing costs, and the advantages of TENG techniques offer diverse sound receiver designs to resolve the stigma. Figure 5A imagines the use of the TAS-based hearing aid for enjoying music. Because of the various material selection and simple structure of TENG techniques, the receiver can be designed as an ear stud for wearing, which is light and artistic (Fig. 5A, inset). Figure 5C illustrates the schematic signal process of our proposed TAS-based hearing aid. The sound information was recorded by the TAS, where because of its resonant property, the signal of the impaired frequency region was naturally enhanced, and then an amplified filter was used for signal processing to a loudspeaker. From the proposed process, TAS works as both sound receiver and certain signal processor of a traditional hearing aid (Fig. 5B). To demonstrate the feasibility of TAS-based hearing aid, first, we assumed that the person's hearing had been impaired to −30 dB in the 207- to 837-Hz and the 1594- to 2090-Hz frequency regions. Through structural design, the hearing aid device in the corresponding resonant frequency region can be prepared. Figure 5D depicts the frequency spectrum of the device, and the related information is also marked. To analog the sound recorded by a person with hearing loss, we treated the original voice by weakening the amplitudes of the frequency regions to −30 dB. Then, the weakened voice was spoken by a loudspeaker, and the TAS-based hearing aid was used to record the sound information. Figure 5E presents the sound wave (top) and the spectrogram (bottom) of the original, weakened, and recorded voices. From the view of frequency domain, the sound information to the impaired frequency region was restored by a TAS-based hearing aid system. Movie S5 also demonstrates the comparison among these three voices. This prototype of a TAS-based hearing aid system shows potential for creating a new type of hearing aid for medical applications.

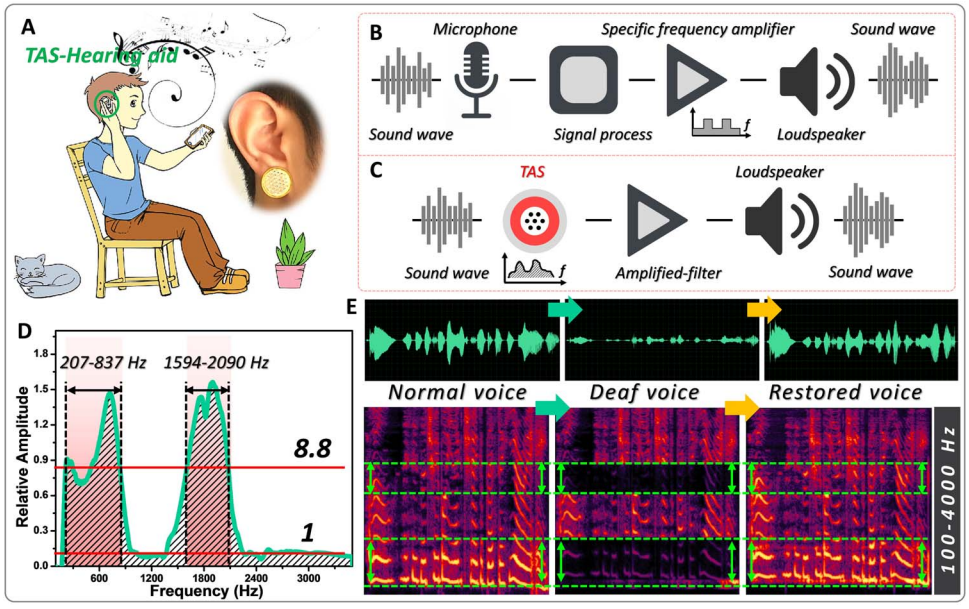

Fig. 5. Medical application of TAS in hearing aids. (**A**) Proposed medical application of TAS in hearing aids to allow a hearing-impaired person to fully hear music. Inset: The TAS-based sound receiver can be worn as ear stud. (**B**) Traditional signal processing of a commercial hearing aid. (**C**) Signal processing of TAS-based hearing aid. TAS is capable of magnifying the specific frequency region. (**D**) Frequency spectrum of a TAS-based hearing aid. The sound response can be magnified 8.8 times for specific frequency band (as marked in the figure) by using a TAS. (**E**) Sound waves and corresponding acoustic spectrograms of normal, weakened, and restored voices. The corresponding frequency bands are marked by green dash lines.

CONCLUSIONS

We have demonstrated a type of electronic auditory platform for social robotics by TENG technology. As the dominant component for robotic audition, triboelectric acoustic sensor exhibited a promising performance with ultrahigh sensitivity and broad-wide frequency response, which may facilitate robot-human social interaction efficiently and precisely. By introducing a geometric boundary, we achieved a tailored frequency response from the sensor itself and showed prospective application for recovering hearing-impaired people, thus complementing human-robot interaction from the human auditory sense. Moreover, triboelectric acoustic sensor is self-powered, single-channel, and cost-efficient, which could reduce power consumption and prolong the robot's operation. With these capabilities, the self-powered perceptual platform based on TENG technology could provide an alternative avenue for addressing future power and social interaction challenges in the development of robotics.

MATERIALS AND METHODS

Fabrication of TAS

The fabrication process of TAS can be divided into preparation of the upper electrode, preparation of the bottom electrode, and assembly of the device. Typically, an acrylic sheet (thickness, 1 mm) was cut into circular pieces (diameter, 15 mm) to act as the upper electrode by using a laser cutter after deposition of an Au layer (200 nm) by vacuum magnetron sputtering. Multiple holes (diameter, 1.2 mm) were created on the substrate to reduce the air damping. Then, a FEP film (thickness, 25 μm) was adhered on the Au layer to work as the tribolayer, and it was then carefully perforated using a needle. To enhance the surface charge density, we used inductively coupled plasma reactive-ion etching to create nanostructure on the FEP surface. Kapton film (thickness, 25, 50, or 75 μm) covered with Au layer (100 nm) was chosen as the vibration membrane and worked as the bottom electrode. Later, an acrylic sheet (thickness, 1 mm) was cut into an annulus (outer diameter, 15 mm; inner diameter, 13 mm) to fix the circumference of the membrane as the outer boundary. A perforated circular acrylic sheet should be used to form the inner boundary frame. Last, the two parts were assembled with a tunable gap in between by using several annular A4 paper (thickness, 100 μm) as the spacer. In addition, various materials such as polyethylene terephthalate, indium tin oxide, graphene, etc. should be used in the fabrication of thin or transparent TAS.

Electric measurement and characterization

Field-emission scanning electron microscopy (Hitachi SU8010) was used to characterize the surface morphology of the nanostructured FEP film. For the electric output measurement of the TENG-based sensor, a sound box (ENKOR E50) with frequency modulation program was used to drive the Kapton membrane to vibrate for quantified investigation. A programmable electrometer (Stanford SR560) was adopted to measure the voltage signal. NI-6259 was used for data collection. The software platform was constructed on the basis of LabVIEW, which is capable of realizing real-time data acquisition control and analysis.

SUPPLEMENTARY MATERIALS

robotics.sciencemag.org/cgi/content/full/3/20/eaat2516/DC1
Supplementary Text
Note S1. Theoretical analysis of the circular membrane.
Note S2. Theoretical analysis of the annular membrane.
Note S3. Theoretical analysis of the sectorial membrane.
Note S4. Effect of resonant cavity on the membrane vibration.
Table. S1. Sound type and corresponding frequency range.
Table. S2. Levels of hearing loss.
Fig. S1. Vibration patterns of circular membrane.
Fig. S2. Potential distribution of TAS.
Fig. S3. Influence of diameter on the frequency spectrum of TAS.
Fig. S4. Influence of thickness on the frequency spectrum of TAS.
Fig. S5. Long-term stability test of TAS.
Fig. S6. Displacement measurement of the membrane.
Fig. S7. Output when miniaturizing the TAS.
Fig. S8. Signal process of the sound switch control electric loop.
Fig. S9. Vibration patterns of annular membrane.
Fig. S10. Finite element analysis of the membrane with annular boundary.
Fig. S11. Vibration patterns of sectorial membrane.
Fig. S12. Finite element analysis of the membrane with sectorial boundary.
Fig. S13. Schematic illustration of the inner boundary structure.
Fig. S14. Effect of single-hole Helmholtz resonator on the frequency response of TAS.
Fig. S15. Effect of multihole Helmholtz resonator on the frequency response of TAS.
Movie S1. TAS as a sensitive sound switch control.
Movie S2. Transparent TAS for antitheft system.
Movie S3. TAS-based high-quantity electronic hearing system.
Movie S4. TAS-based voice recognition system.
Movie S5. TAS-based new type of hearing aid system.

REFERENCES AND NOTES

1. G.-Z. Yang, J. Bellingham, P. E. Dupont, P. Fischer, L. Floridi, R. Full, N. Jacobstein, V. Kumar, M. McNutt, R. Merrifield, B. J. Nelson, B. Scassellati, M. Taddeo, R. Taylor, M. Veloso, Z. L. Wang, R. Wood, The grand challenges of *Science Robotics*. *Sci. Robot.* **3**, eaar7650 (2018).
2. H. Admoni, B. Scassellati, Social eye gaze in human-robot interaction: A review. *J. Hum. Robot Interact.* **6**, 25–63 (2017).
3. B. Scassellati, Theory of mind for a humanoid robot. *Auton. Robot.* **12**, 13–24 (2002).
4. N. Oishi, J. Schacht, Emerging treatments for noise-induced hearing loss. *Expert Opin. Emerg. Drugs* **16**, 235–245 (2011).
5. B. O. Olusanya, K. J. Neumann, J. E. Saunders, The global burden of disabling hearing impairment: A call to action. *Bull. World Health Organ.* **92**, 367–373 (2014).
6. M. M. Popelka, K. J. Cruickshanks, T. L. Wiley, T. S. Tweed, B. E. K. Klein, R. Klein, Low prevalence of hearing aid use among older adults with hearing loss: The epidemiology of hearing loss study. *J. Am. Geriatr. Soc.* **46**, 1075–1078 (1998).
7. C. Meyer, L. Hickson, What factors influence help-seeking for hearing impairment and hearing aid adoption in older adults? *Int. J. Audiol.* **51**, 66–74 (2012).
8. M. Tate, The hearing aid system, in *Principles of Hearing Aid Audiology* (Springer, 1994), pp. 73–94.
9. S. Launer, J. A. Zakis, B. C. J. Moore, Hearing aid signal processing, in *Hearing Aids*, G. R. Popelka, B. C. J. Moore, R. R. Fay, A. N. Popper, Eds. (Springer International Publishing, 2016), pp. 93–130.
10. E. Villchur, Signal processing to improve speech intelligibility in perceptive deafness. *J. Acoust. Soc. Am.* **53**, 1646–1657 (1973).
11. M. Wehner, R. L. Truby, D. J. Fitzgerald, B. Mosadegh, G. M. Whitesides, J. A. Lewis, R. J. Wood, An integrated design and fabrication strategy for entirely soft, autonomous robots. *Nature* **536**, 451–455 (2016).
12. M. Boyvat, J.-S. Koh, R. J. Wood, Addressable wireless actuation for multijoint folding robots and devices. *Sci. Robot.* **2**, eaan1544 (2017).
13. J. Jang, J. Lee, S. Woo, D. J. Sly, L. J. Campbell, J.-H. Cho, S. J. O'Leary, M.-H. Park, S. Han, J.-W. Choi, J. H. Jang, H. Choi, A microelectromechanical system artificial basilar membrane based on a piezoelectric cantilever array and its characterization using an animal model. *Sci. Rep.* **5**, 12447 (2015).
14. H. S. Lee, J. Chung, G.-T. Hwang, C. K. Jeong, Y. Jung, J.-H. Kwak, H. Kang, M. Byun, W. D. Kim, S. Hur, S.-H. Oh, K. J. Lee, Flexible inorganic piezoelectric acoustic nanosensors for biomimetic artificial hair cells. *Adv. Funct. Mater.* **24**, 6914–6921 (2014).
15. J. Jang, S. Kim, D. J. Sly, S. J. O'Leary, H. Choi, MEMS piezoelectric artificial basilar membrane with passive frequency selectivity for short pulse width signal modulation. *Sens. Actuators A Phys.* **203**, 6–10 (2013).
16. S. Kim, W. J. Song, J. Jang, J. H. Jang, H. Choi, Mechanical frequency selectivity of an artificial basilar membrane using a beam array with narrow supports. *J. Micromech. Microeng.* **23**, 095018 (2013).
17. W. C. Jones, L. W. Giles, A moving coil microphone for high quality sound reproduction. *J. Soc. Motion Pic. Eng.* **17**, 977–993 (1931).
18. S. C. B. Mannsfeld, B. C.-K. Tee, R. M. Stoltenberg, C. V. H.-H. Chen, S. Barman, B. V. O. Muir, A. N. Sokolov, C. Reese, Z. Bao, Highly sensitive flexible pressure sensors with microstructured rubber dielectric layers. *Nat. Mater.* **9**, 859–864 (2010).
19. M. Li, H. X. Tang, M. L. Roukes, Ultra-sensitive NEMS-based cantilevers for sensing, scanned probe and very high-frequency applications. *Nat. Nanotechnol.* **2**, 114 (2007).
20. F.-R. Fan, Z.-Q. Tian, Z. L. Wang, Flexible triboelectric generator. *Nano Energy* **1**, 328–334 (2012).
21. Y. Zi, S. Niu, J. Wang, Z. Wen, W. Tang, Z. Lin Wang, Standards and figure-of-merits for quantifying the performance of triboelectric nanogenerators. *Nat. Commun.* **6**, 8376 (2015).
22. Z. L. Wang, Triboelectric nanogenerators as new energy technology and self-powered sensors—Principles, problems and perspectives. *Faraday Discuss.* **176**, 447–458 (2014).
23. Y. Zi, J. Wang, S. Wang, S. Li, Z. Wen, H. Guo, Z. L. Wang, Effective energy storage from a triboelectric nanogenerator. *Nat. Commun.* **7**, 10987 (2016).
24. Z. L. Wang, On Maxwell's displacement current for energy and sensors: The origin of nanogenerators. *Mater. Today* **20**, 74–82 (2017).
25. A. Li, Y. Zi, H. Guo, Z. L. Wang, F. M. Fernández, Triboelectric nanogenerators for sensitive nano-coulomb molecular mass spectrometry. *Nat. Nanotechnol.* **12**, 481–487 (2017).
26. J. Wang, S. Li, F. Yi, Y. Zi, J. Lin, X. Wang, Y. Xu, Z. L. Wang, Sustainably powering wearable electronics solely by biomechanical energy. *Nat. Commun.* **7**, 12744 (2016).
27. Z. Wen, M.-H. Yeh, H. Guo, J. Wang, Y. Zi, W. Xu, J. Deng, L. Zhu, X. Wang, C. Hu, L. Zhu, X. Sun, Z. L. Wang, Self-powered textile for wearable electronics by hybridizing

fiber-shaped nanogenerators, solar cells, and supercapacitors. *Sci. Adv.* **2**, e1600097 (2016).
28. Z. L. Wang, T. Jiang, L. Xu, Toward the blue energy dream by triboelectric nanogenerator networks. *Nano Energy* **39**, 9–23 (2017).
29. J. Chen, Y. Huang, N. Zhang, H. Zou, R. Liu, C. Tao, X. Fan, Z. L. Wang, Micro-cable structured textile for simultaneously harvesting solar and mechanical energy. *Nat. Energy* **1**, 16138 (2016).
30. Y. Zi, H. Guo, Z. Wen, M.-H. Yeh, C. Hu, Z. Lin Wang, Harvesting low-frequency (<5 Hz) irregular mechanical energy: A possible killer application of triboelectric nanogenerator. *ACS Nano* **10**, 4797–4805 (2016).
31. S. Niu, X. Wang, F. Yi, Y. S. Zhou, Z. L. Wang, A universal self-charging system driven by random biomechanical energy for sustainable operation of mobile electronics. *Nat. Commun.* **6**, 8975 (2015).
32. X. Pu, H. Guo, J. Chen, X. Wang, Y. Xi, C. Hu, Z. L. Wang, Eye motion triggered self-powered mechnosensational communication system using triboelectric nanogenerator. *Sci. Adv.* **3**, e1700694 (2017).
33. J. Yang, J. Chen, Y. Su, Q. Jing, Z. Li, F. Yi, X. Wen, Z. Wang, Z. L. Wang, Eardrum-inspired active sensors for self-powered cardiovascular system characterization and throat-attached anti-interference voice recognition. *Adv. Mater.* **27**, 1316–1326 (2015).
34. S. Wang, L. Lin, Z. L. Wang, Triboelectric nanogenerators as self-powered active sensors. *Nano Energy* **11**, 436–462 (2015).
35. J. Chen, H. Guo, J. Zheng, Y. Huang, G. Liu, C. Hu, Z. L. Wang, Self-powered triboelectric micro liquid/gas flow sensor for microfluidics. *ACS Nano* **10**, 8104–8112 (2016).
36. X. Pu, M. Liu, X. Chen, J. Sun, C. Du, Y. Zhang, J. Zhai, W. Hu, Z. L. Wang, Ultrastretchable, transparent triboelectric nanogenerator as electronic skin for biomechanical energy harvesting and tactile sensing. *Sci. Adv.* **3**, e1700015 (2017).
37. Y. S. Zhou, G. Zhu, S. Niu, Y. Liu, P. Bai, Q. Jing, Z. L. Wang, Nanometer resolution self-powered static and dynamic motion sensor based on micro-grated triboelectrification. *Adv. Mater.* **26**, 1719–1724 (2014).
38. X. Fan, J. Chen, J. Yang, P. Bai, Z. Li, Z. L. Wang, Ultrathin, rollable, paper-based triboelectric nanogenerator for acoustic energy harvesting and self-powered sound recording. *ACS Nano* **9**, 4236–4243 (2015).
39. J. Jang, J. Lee, J. H. Jang, H. Choi, A triboelectric-based artificial basilar membrane to mimic cochlear tonotopy. *Adv. Healthc. Mater.* **5**, 2481–2487 (2016).
40. P. M. Morse, K. U. Ingard, Theoretical acoustics. *Am. J. Phys.* **38**, 666–667 (1970).
41. D. K. Davies, Charge generation on dielectric surfaces. *J. Phys. D. Appl. Phys.* **2**, 1533 (1969).
42. A. R. J. Murray, I. R. Summers, J. R. Sambles, A. P. Hibbins, An acoustic double fishnet using Helmholtz resonators. *J. Acoust. Soc. Am.* **136**, 980–984 (2014).

Funding: This work was supported by National Natural Science Foundation of China (NSFC) (51572040 and 51772036), the Chongqing University Postgraduates' Innovation Project (grant no. CYB17044), NSFC (61774016), and the Natural Science Foundation Project of Chongqing (cstc2015jcyjA20020 and cstc2017jcyjAX0307). **Author contributions:** H.G., X.P., J.C., C.H., J.W., and Z.L.W. conceived the idea and designed the TAS. H.G., X.P., and J.C. fabricated the TAS, designed, and performed the experiments. H.G., J.W., C.H., and Z.L.W. analyzed the data and prepared the manuscript. All authors discussed the results and commented on the manuscript. **Competing interests:** The authors declare that they have no competing interests. **Data and materials availability:** All data used to obtain the conclusions in this paper are presented in the paper and/or the Supplementary Materials. Please contact H.G., X.P., and J.C. for data and other materials.

Submitted 8 February 2018
Accepted 3 July 2018
Published 25 July 2018
10.1126/scirobotics.aat2516

Citation: H. Guo, X. Pu, J. Chen, Y. Meng, M.-H. Yeh, G. Liu, Q. Tang, B. Chen, D. Liu, S. Qi, C. Wu, C. Hu, J. Wang, Z. L. Wang, A highly sensitive, self-powered triboelectric auditory sensor for social robotics and hearing aids. *Sci. Robot.* **3**, eaat2516 (2018).

Science Robotics

A highly sensitive, self-powered triboelectric auditory sensor for social robotics and hearing aids

Hengyu Guo, Xianjie Pu, Jie Chen, Yan Meng, Min-Hsin Yeh, Guanlin Liu, Qian Tang, Baodong Chen, Di Liu, Song Qi, Changsheng Wu, Chenguo Hu, Jie Wang and Zhong Lin Wang

Sci. Robotics **3**, eaat2516.
DOI: 10.1126/scirobotics.aat2516